THE JOURNAL OF PHYSICAL CHEMISTRY B
A JOURNAL OF THE AMERICAN CHEMICAL SOCIETY

pubs.acs.org/JPCB

Article

Impedance Spectroscopy Dynamics of Biological Neural Elements: From Memristors to Neurons and Synapses

Published as part of The Journal of Physical Chemistry virtual special issue "125 Years of The Journal of Physical Chemistry".

Agustín Bou and Juan Bisquert*

Cite This: https://doi.org/10.1021/acs.jpcb.1c03905

Read Online

ACCESS | Metrics & More | Article Recommendations | Supporting Information

ABSTRACT: Understanding the operation of neurons and synapses is essential to reproducing biological computation. Building artificial neuromorphic networks opens the door to a new generation of faster and low-energy-consuming electronic circuits for computation. The main candidates to imitate the natural biocomputation processes, such as the generation of action potentials and spiking, are memristors. Generally, the study of the performance of material neuromorphic elements is done by the analysis of time transient signals. Here, we present an analysis of neural systems in the frequency domain by small-amplitude ac impedance spectroscopy. We start from the constitutive equations for the conductance and memory effect, and we derive and classify the impedance spectroscopy spectra. We first provide a general analysis of a memristor and demonstrate that this element can be expressed as a combination of simple parts. In particular, we derive a basic equivalent circuit where the memory effect is represented by an RL branch. We show that this ac model is quite general and describes the inductive/negative capacitance response in many systems such as halide perovskites and organic LEDs. Thereafter, we derive the impedance response of the integrate-and-fire exponential adaptative neuron model that introduces a negative differential resistance and a richer set of spectra. On the basis of these insights, we provide an interpretation of the varied spectra that appear in the more general Hodgkin–Huxley neuron model. Our work provides important criteria to determine the properties that must be found in material realizations of neuronal elements. This approach has the great advantage that the analysis of highly complex phenomena can be based purely on the shape of experimental impedance spectra, avoiding the need for specific modeling of rather involved material processes that produce the required response.

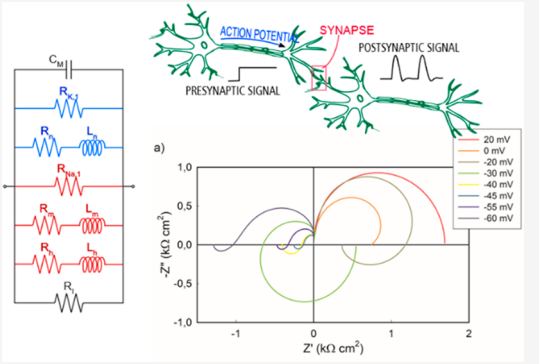

1. INTRODUCTION

Biological intelligence colocalizes memory and computing, enabling the brain to carry out robust and efficient parallel computation with extremely low power consumption. Neuromorphic networks consist of large arrays of nanoscale inorganic and hybrid material components. They can reach high levels of integration density to provide compact low-power electronic circuits for autonomous intelligence adapted to buildings, vehicles, and equipment.[1−6] These bioinspired artificial computation networks open the opportunity to overcome the Von-Neumann bottleneck related to the time and energy spent transporting data between memory and processor.[7]

Neurons and synapses are the main elements of biological computation. Neurons operate by gating mechanisms controlled by voltage-gated ion channels that modify the membrane potentials. Voltage-gated sodium channels are proteins which transfer sodium ions across the membrane depending on the electrochemical potential gradient controlled by the transmembrane difference in ion concentration. Opening of the sodium channel results in an increased electrochemical potential inside the membrane and leads to depolarization. When the potential exceeds a positive threshold value, there is a positive feedback of Na^+ influx that provokes a large depolarization burst termed the action potential. At the same time, voltage-gated potassium channels become activated and produce an outward flux of K^+ that leads to the repolarization completing a negative feedback loop. Neurons realize communication with these electrical signals by receiving trains of voltage spikes at synapses, integrating these inputs, and firing spikes consisting of repetitive action potentials in turn. The synapses are able to change the strength of

Received: May 1, 2021
Revised: July 16, 2021

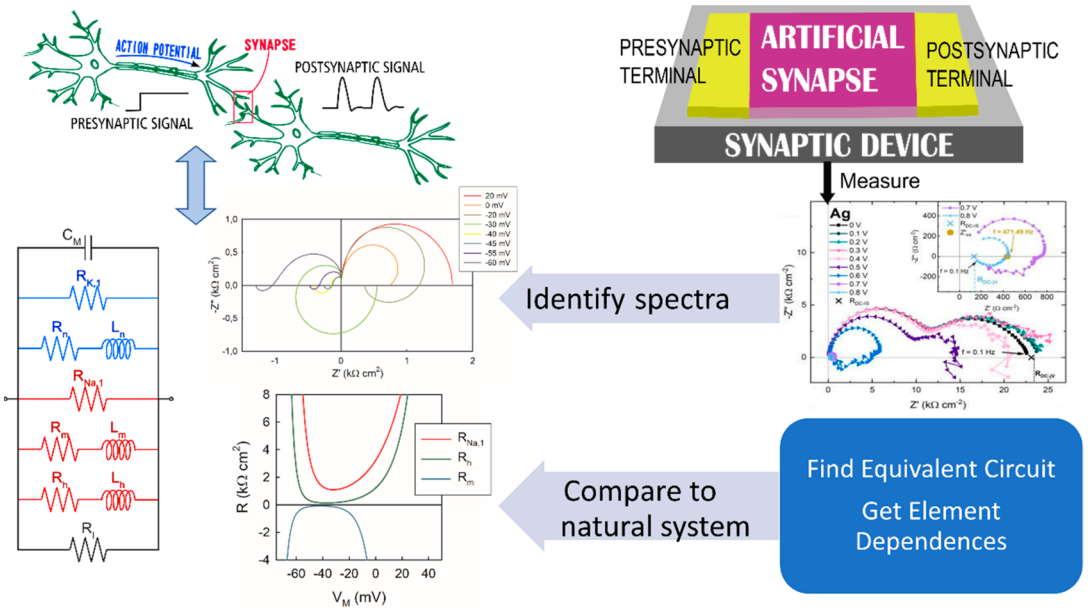

Figure 1. Scheme for the IS analysis of artificial synaptic/neuronal devices (right) with respect to the response of the natural synapsis or neuron (left).

connectivity, which regulates biological learning, memory, and analog computation. The synchronicity of spike trains produces either a potentiation or depression of synaptic weights, in the spike-timing-dependent plasticity which occurs as a short-time plasticity or long-time plasticity mechanism, according to the duration of the change. Additional mechanisms of learning are the Hebbian correlational learning, reinforcement, habituations, and others.

Understanding the mechanisms of the generation of action potentials, spiking, and the adjustment of the weights of connections in time-dependent plasticity and learning mechanisms are the basic building blocks to realize the neuromorphic computation. For the construction of spiking neural networks that mimic the neuronal style of computation, it is necessary to build basic material components and circuits that emulate the underlying biophysical switching mechanisms of neurons and synapses and reproduce their detailed real-time dynamics.[2,8−10] The temporal response of the electrical signal in terms of the biological structure has been well described by a variety of models, from the integrate-and-fire model to the Hodgkin−Huxley model.[11−13] These models provide a fundamental target reference to reproduce the time dynamics with material components. There have been intensive efforts to build an electronic device with properties similar to the Hodgkin−Huxley axon, denominated neuristor.[14]

To obtain a fundamental understanding of the dynamic response of neurons and synapses, here we propose that important insight can be gained by analyzing the candidate material elements in the frequency domain, as outlined in Figure 1.

In the next section, we explain important basic aspects of the technique of impedance spectroscopy (IS) and lay out the general tasks of the method proposed. Thereafter, we will follow a ladder of increasing complexity, starting with the analysis of elementary memristors and then addressing the IS response of the models for neurons, first for the two variable adaptative integrate-and-fire models and then for the four-dimensional Hodgkin−Huxley model that describes the operation of neuron spiking by the concerted actions of the sodium and potassium ion channels.

2. IMPEDANCE SPECTROSCOPY

2.1. Introduction to Impedance Spectroscopy. The technique of small-amplitude IS is widely used in electrochemistry and materials science to determine the electrical response of a system.[15,16] It is an important tool for the characterization of emergent solar cells[16,17] and perovskite solar cells.[18−20] It is also used for many applications in biophysics[21,22] such as research in cells,[23] antimicrobials,[24] medicine and healthcare,[25,26] and biosensorics.[27] The impedance of the intrinsic neuronal response determines the cooperation in a network.[28]

The impedance is measured by a small perturbation over a steady state at angular frequency ω, and it can be presented in terms of the real and imaginary parts

$$Z(\omega) = Z'(\omega) + iZ''(\omega) \quad (1)$$

The complex capacitance $C(\omega)$ is defined from the impedance as

$$C(\omega) = \frac{1}{i\omega Z(\omega)} \quad (2)$$

It can be separated into real and imaginary parts as

$$C(\omega) = C'(\omega) - iC''(\omega) \quad (3)$$

When we study the impedance response of any system, we aim to find the equivalent circuit (EC) that best describes the impedance spectra generated by the system to extract all of the information provided by the spectra. Therefore, determining which is the EC of the system we are studying is key to having a satisfactory analysis and a proper interpretation of the measurements. IS gives insight about physical properties and mechanisms: given the type of spectra and EC model, one can learn about the system that generated it.

The impedance measured in a system is not constant, and the spectra evolve as we change the applied voltage. This is not

https://doi.org/10.1021/acs.jpcb.1c03905
J. Phys. Chem. B XXXX, XXX, XXX−XXX

a problem since a single EC with variable elements is able to reproduce a wide variety of spectra, as we will see in Section 2.2. These variable elements hold valuable information about the operation of the systems; therefore, knowing which is the dependence of the elements with voltage is key to uncovering internal mechanisms.

To clarify this method, we show an example of measured impedance spectra in a perovskite solar cell at different applied voltages from previous work in Figure 2a.[29] This set of spectra

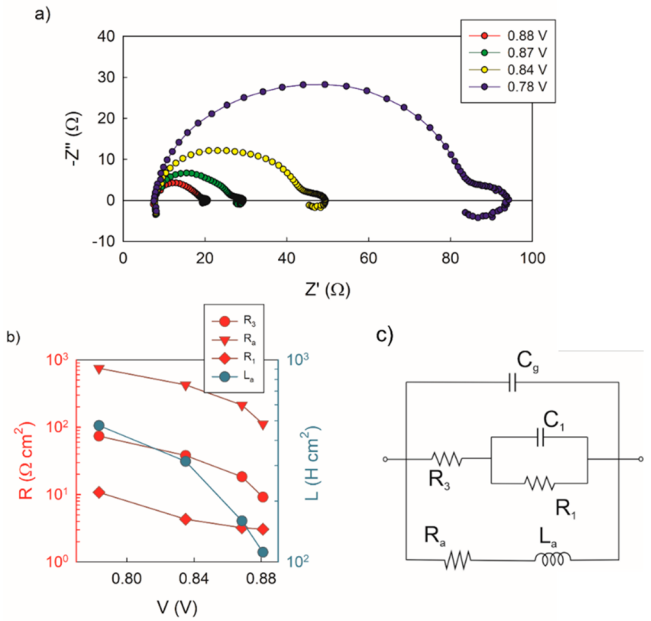

Figure 2. (a) Impedance complex plane plot of a perovskite solar cell at different applied voltages fitted with the same EC. (b) Extracted resistances from (c) the fitting showing an exponential dependence. Adapted from ref 29.

are fitted with the EC shown in Figure 2c. It is observed that the elements of the circuit are not constant; in fact, they vary with the applied voltage. Figure 2b shows the exponential variation of both resistances and the inductor with voltage, which is a common behavior in solar cell devices.

When a satisfactory EC model has been found, one has to take into account that there are several alternative arrangements that describe the same model.[30] The selection of the EC needs to be done on the basis of the physical interpretation of the elements and the experimentation of a variety of samples with different morphologies and material combinations.

2.2. IS Model with Capacitor and Inductor. We show the complete analysis of an EC containing a capacitor and an inductor. It will be shown later that this model is representative of a simple memristor and is of interest for the subsequent analysis of neuron models. In this section, we will see the shape of the spectra depending on the values of the elements of the circuit. Later, we will carry out a further analysis considering the parameters of the kinetic models that govern the elements of the circuit.

The circuit that we are going to use is represented in Figure 3. The impedance generated by this circuit is

$$Z(\omega) = [R_b^{-1} + C_m s + (R_a + L_a s)^{-1}]^{-1} \quad (4)$$

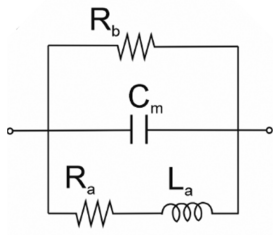

Figure 3. Equivalent circuit with an inductor and a capacitor, representative of a memristor.

Here $s = i\omega$. The circuit is able to generate a wide variety of spectra, depending on the relation between the elements of the circuit.

The dc resistance of the circuit, which is a key parameter in the shape of the spectra, can be calculated as

$$R_{dc} = \left(\frac{1}{R_a} + \frac{1}{R_b}\right)^{-1} \quad (5)$$

First, we consider the case where both resistances in the EC are positive. Therefore, R_{dc} will be positive. In this case, we have two possibilities depending on whether the spectra cross the real axis. These spectra are shown in Figure 4, indicating the relation between some of the elements and the time constant τ_k, characteristic of the RL branch and defined as

$$\tau_k = \frac{L_a}{R_a} \quad (6)$$

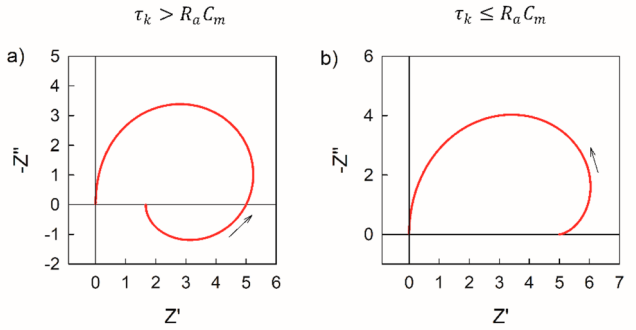

Figure 4. Complex plane impedance spectra for EC in Figure 3. (a) $R_a = 2$, $R_b = 10$, $C_m = 10$, and $L_a = 200$. (b) $R_a = 10$, $R_b = 10$, $C_m = 10$, and $L_a = 1000$. The arrow indicates the direction of increasing frequency.

When τ_k is greater than the product R_aC_m, we get a spectrum of the type in Figure 4a, i.e., an arc in the first quadrant that loops into the fourth quadrant. Otherwise, we obtain the spectrum in Figure 4b, an arc in the first quadrant that can loop or not but never goes into the fourth quadrant.

We now look at the conditions for having a positive dc resistance but a spectrum that crosses the imaginary axis. This means that there will be a region where the real part of the impedance is negative, although the total resistance of the circuit R_{dc} is positive. The condition for the impedance to cross the imaginary axis is

$$-R_a > R_b \quad (7)$$

https://doi.org/10.1021/acs.jpcb.1c03905
J. Phys. Chem. B XXXX, XXX, XXX−XXX

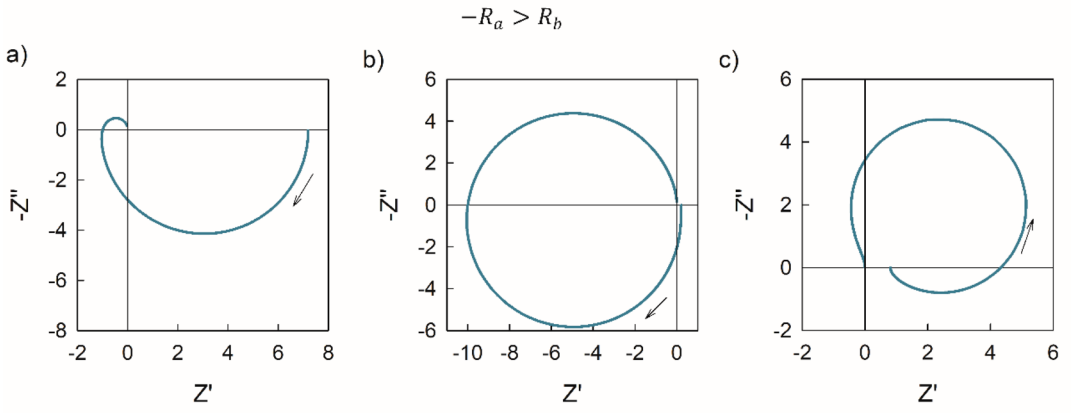

Figure 5. Complex plane impedance spectra for EC in Figure 3, where the dc resistance is $R_{dc} > 0$ and the condition for hidden negative impedance is satisfied. (a) $R_a = 0.8$, $R_b = -9$, $R_{dc} = 7.2$, $C_m = 10$, and $L_a = 80$. (b) $R_a = 0.2$, $R_b = -5$, $R_{dc} = 0.2083$, $C_m = 10$, and $L_a = 20$. (c) $R_a = 0.5$, $R_b = -1.3$, $R_{dc} = 0.81$, $C_m = 100$, and $L_a = 50$. The arrow indicates the direction of increasing frequency.

This means that one or both resistances must be negative. However, to maintain the condition that the dc resistance is positive, we need one of the resistances to be positive. This kind of spectrum has a part of the real impedance on the real negative side, although the impedance at zero frequency is positive. This is defined by Koper as the "hidden negative impedance",[31−33] and it is a condition for the generation of spiking signals. Therefore, we show three examples of this kind of spectrum in Figure 5 since the observation of a spectrum of this kind is key to building artificial neuron devices.

Finally, we show two examples of spectra with negative R_{dc}, which means that the impedance at zero frequency will be negative. As we can see in Figure 6, this can be achieved with only one of the resistances being negative. As in Figure 4, when $\tau_k > R_aC_m$ (Figure 6a), the real axis is crossed; otherwise (Figure 6b), it is not.

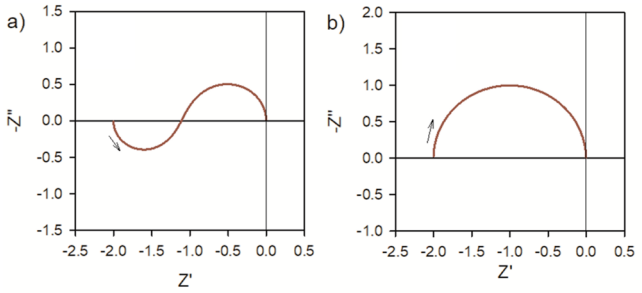

Figure 6. Complex plane impedance spectra for EC in Figure 3, with $R_{dc} < 0$. (a) $R_a = 2$, $R_b = -1$, $R_{dc} = -2$, $C_m = 10$, $L_a = 200$. (b) $R_a = 2$, $R_b = -1$, $R_{dc} = -2$, $C_m = 100$, $L_a = 20$. The arrow indicates the direction of increasing frequency.

As we have seen in the different figures, the spectral features generated by the circuit in Figure 3 are diverse. The model takes into account different possible shapes according to the impedance parameters. The classification of patterns depending on physical parameters will be made in Section 3, where we attach specific meaning to the EC elements based on a physical model. A full interpretation of the EC and model parameters is presented in the Supporting Information.

2.3. Impedance Spectroscopy as a Tool to Emulate Natural Neural Elements. The principal feature of the technique of IS is that the frequency is scanned over many decades and the consequent spectral response of the impedance provides specific information about the dominant resistive-capacitive processes in the sample. Traditionally, IS gives insight about physical properties: given a type of spectra and EC model, what can we learn from the system that generated it?

In this article, we aim to establish the dominant IS characteristics of biological neural elements for computation, learning, and artificial intelligence. The identification of impedance behavior provides a benchmark for the construction of material devices with the dynamic properties akin to natural neurons. In particular, here we find inspiration in the theory of electrochemical oscillations based on impedance criteria that have been developed by Koper using the methods of electrical control engineering.[31,34] It is remarkable that from the shape of the experimental impedance spectra one may analyze extremely complex phenomena without the need for the specific modeling of highly involved material processes that produce the physical response of interest.

On the basis of the operational understanding at the EC level, we can ensure that an artificial system delivers the same operation as the natural system to copy. Then, for the construction of a device that can perform as an artificial neuron we need a system that reproduces the frequency domain behavior of the target application. We can measure the impedance of the device and identify the possible similarities with the impedance response of the natural system, finding responses with similar ECs. We can adjust the different internal kinetic elements until we obtain the specific desired outcome.

At the single-device level, we can obtain deep insight about the required responses. At present, extensive data on the IS of neurons is not available, but the desired frequency domain response can be obtained by the analysis of the models that reproduce the natural neuron response in the time domain, such as the adaptative integrate-and-fire, the FitzHugh−Nagumo model and the Hodgkin−Huxley model.

A scheme of the method that is to be followed for the analysis of artificial synaptic devices is shown in Figure 1. Here, on the left we have represented the natural presynaptic neurons and a synapse with the spiking postsynaptic responses. Below, we represent the catalogue of spectra produced by the EC generated by the Hodgkin−Huxley model as well as the values of the variable resistances of the model. Knowing the possible shapes of the spectra, we need to measure impedances

https://doi.org/10.1021/acs.jpcb.1c03905
J. Phys. Chem. B XXXX, XXX, XXX−XXX

in our intended neural devices and just identify the shapes found in the natural systems. Furthermore, we need to find an EC similar to that of the natural system and get similar dependences.

In the case of electrochemical oscillations and similar systems, the impedance response is associated with negative differential resistance (NDR) elements and also negative capacitance and inductive features. The pioneering work of Chua and co-workers[35,36] showed that the spiking of neurons operates in unstable regions according to the bifurcation theory that can be visualized by the stability criteria of impedance and admittance ("the edge of chaos"). A better comprehension of the dynamic role of these unfamiliar negative elements may form an important tool for the rapid diagnosis and assessment of the properties of material systems that are candidates for artificial neurons. Our method relies on a classification of ECs associated with neuron models.

In artificial spiking neural networks, the analog signals collected from the environment need to be converted to spiking signals with dynamic oscillation frequencies.[8] In synapses, the input frequency of the signal modulates the conductivity.[37] In neurons, the spike frequency increases with increased stimulus strength.[9] The connection between the output spiking frequency and the internal characteristic frequencies in the EC of the neuron must hold a deep connection. The dynamic spiking behavior under various input signals, such as rectangular, triangular, and sinusoidal pulses, needs to be investigated on the basis of EC properties. One expects to find universality close to a critical point of the dynamic system, but not close to a fixed point. This topic is left for future investigations.

3. MEMRISTORS

3.1. Fundamental Properties of Memristors. At the present time, the main resource for building neuromorphic networks is memristors.[38−40] A memristive device is a two-terminal structure that undergoes a voltage-controlled conductance change.[41] When the memristor is adapted as a neuron, it has to integrate a pulse train and generate a voltage spike when a certain voltage is exceeded. On the other hand, for the use of a memristor as a synapse, it has to be programmed at distinct nonvolatile resistive states to support spike-timing-dependent plasticity.[42−45]

There are a wide variety of types of memristors suitable for bioinspired computational networks including silicon oxides,[46] silicon nitrides,[47] and metal oxides.[48,49] The hybrid and organic electronic materials provide mechanical flexibility and biocompatibility, enabling the formation of neuromorphic systems that can be smoothly interfaced to biological interfaces for the reception of stimuli.[4,50,51] The metal halide perovskites[52−57] are an emergent class of photovoltaic materials that have the advantage of easy fabrication and the properties of a mixed ionic−electronic conductor, with strong hysteresis effects induced by the slow ion motions. This ionic adaptation to an external stimulus opens a significant opportunity to replicate the switching responses occurring in ionic channels of biological neural units. In practice, however, emulating the neurons, synapses, and their networks using ionic−electronic elements is extraordinarily challenging due to the involved structure and multifunctionality of the biological elements, with highly complex responses that are usually studied in the time domain.

3.2. Basic Kinetic Equations of a General Memristor. The memristor is a resistive element where the resistance depends on the history of one or more of the state variables of the system. The state variables are those variables necessary to determine the future behavior of a system when the present state of the system and the inputs are known.[58] In the context of memristors, a state variable is associated with the device material internal elements and its operation. The state variables must not be influenced independently by external variables such as a voltage or current applied to a third terminal.[59]

In terms of voltage u, current I, and the internal variable w, the current−voltage characteristic is therefore determined by two constitutive equations of the type[41]

$$I = G(w, u)u \tag{8}$$

$$\tau_k \frac{dw}{dt} = g(w, u) \tag{9}$$

Here, τ_k is a time constant for the relaxation of state variable w to an equilibrium dictated by the value of u. In the standard definition of a memristor, the characteristic current−voltage shape when excited by a bipolar periodic stimulus (that goes from positive to negative voltage) is a pinched hysteresis loop that occurs in the first and the third quadrants of the $I-u$ plane, passing through the origin since $I = 0$ at $u = 0$. Often in the literature the denomination of an ideal memristor (in which the state variable is the voltage flux) is applied only to systems that have the only equilibrium point $\dot{w} = 0$ at the origin at $u = 0$,[59] as in eq 22. To investigate the IS characteristics, here we take the more general denomination associated with memristors, in which $g(w, u) = 0$ allows other operation points along the current−voltage curve. In the neuron models eq 8 contains terms that do not depend on u, see eq 26.

When the system is left to a steady state (a stable point), we obtain a curve $\bar{I} = G(\bar{u})\bar{u}$ according to the applied voltage, where the overbar denotes the value at steady state. An example is shown later in eq 29. Now we investigate the dynamics at a specific point.

To calculate the impedance response of the general model, in eqs 8 and 9 we expand the terms for a small perturbation at steady state, indicating the small perturbation value by a tilde. We also take the Laplace transform of eq 9, $d/dt \to s$. We get a set of linear equations that contain the local information about the system:

$$\tilde{I} = G_w \bar{u}\tilde{w} + (\bar{G} + G_u \bar{u})\tilde{u} \tag{10}$$

$$\tau_k s\tilde{w} = g_w \tilde{w} + g_u \tilde{u} \tag{11}$$

The subscript denotes the partial derivative. Equations 10 and 11 are also used in bifurcation theory to find the stability properties of the fixed points, as we comment on later in eq 35.

To obtain an EC representation of the dynamics of the system, let us define the following electrical elements, two resistances

$$R_b = (\bar{G} + G_u \bar{u})^{-1} \tag{12}$$

$$R_a = -\frac{g_w}{G_w g_u \bar{u}} \tag{13}$$

and an inductor

https://doi.org/10.1021/acs.jpcb.1c03905
J. Phys. Chem. B XXXX, XXX, XXX−XXX

$$L_a = \frac{\tau_k}{G_w g_u \bar{u}} \tag{14}$$

From eqs 13 and 14, we can see that τ_k in a memristor matches with τ_k in eq 6 when $g_w = -1$. We obtain the impedance

$$Z(\omega) = \frac{\tilde{u}}{\tilde{I}} = [R_b^{-1} + (R_a + L_a s)^{-1}]^{-1} \tag{15}$$

The EC formed by a resistive branch and an *RL* branch is indicated in Figure 7A.

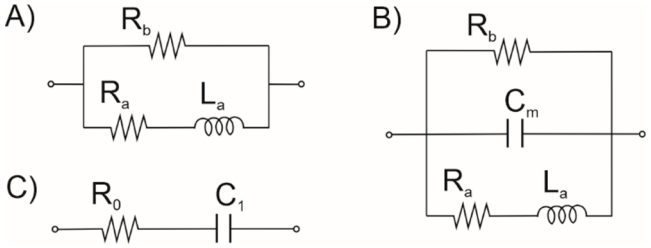

Figure 7. Equivalent circuits for general memristor models.

Now we introduce another factor into the constitutive equations. This is not included in the canonical definition of the memristor; however, it is relevant to IS studies since in many material systems the variation of voltage is influenced by the charging of capacitors in addition to the conduction currents.

We extend the previous model as follows

$$\tau_m \frac{du}{dt} = R_I[I - G(w, u)u] \tag{16}$$

$$\tau_k \frac{dw}{dt} = g(w, u) \tag{17}$$

The charging capacitance is

$$C_m = \frac{\tau_m}{R_I} \tag{18}$$

and the impedance becomes that of eq 4, that we repeat here for convenience

$$Z(\omega) = [R_b^{-1} + C_m s + (R_a + L_a s)^{-1}]^{-1} \tag{19}$$

The charging feature adds the capacitive line to the EC, as shown in Figure 7B.

We suggest the EC of Figure 7B to be the reference behavior for memristor dynamics, which is of the same type as the one in Figure 3. In the literature, we find that this circuit was first described for a model of hydrogen oscillations on a platinum electrode,[31] which indicates that the model in eqs 16 and 17 is quite general and has been expressed in electrochemistry. We will see another version of this model corresponding perfectly to an integrate-and-fire neuron in the next section. In fact, the memristive model of eqs 16 and 17 belongs to the general class of *fast-slow systems*, like the van der Pol oscillator or the FitzHugh–Nagumo neuron model. One can guess that the EC of Figure 3 is a general feature of these and other fast-slow dynamical systems. If the charging is extremely fast ($\tau_m \to 0$), then the model returns to eq 8 and the capacitor effect vanishes.

Our analysis of the small ac perturbation shows that the memristor can be represented by a combination of standard circuit elements. In contrast to the original suggestion,[38] the memristor cannot be considered to be a fundamental circuit element on equal footing with a resistor, capacitor, and inductor, at least for the small ac impedance response. This problem has been discussed before.[60]

It is important to emphasize the dynamic response associated with the memory effect in this model, which can be seen in Figure 4. In principle, the model indicates a single regular relaxation with a resistance R_b. However, it is clear that the dc resistance is smaller since the parallel branch R_a reduces the final resistance. The memory effect associated with the *w* equation in the memristor is indicated by the inductor. At high frequency, the impedance of the inductor is very large and R_a does not contribute to the response. However, when the frequency is reduced, this branch becomes active and reduces the overall resistance of the system by the loop in the fourth quadrant. A full analysis of hysteresis in current–voltage curves in this model has been presented recently.[61]

3.3. Lead Halide Perovskite Memristor and Other Material Systems with Inductive Memristor Behavior. An example of the characteristic action of a perovskite memristor is shown in Figure 8. When the voltage is scanned

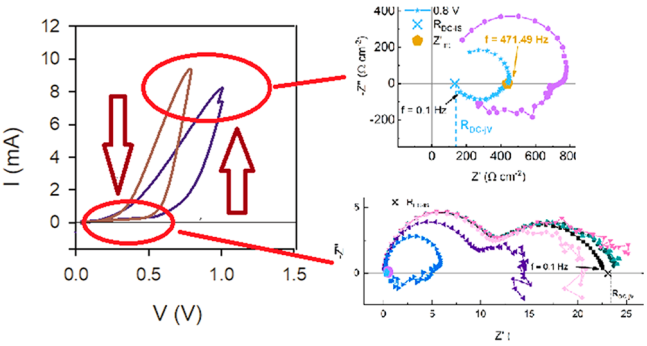

Figure 8. (Left) Current–voltage curve of a FTO/PEDOT:PSS/2D Ruddlesden–Popper perovskite/Ag (15 nm)/Au (85 nm) memristor device showing the transition from a high resistance state to a low resistance state. (Right) IS spectral evolution of the memristor at representative voltages. Reproduced from ref 33.

over a certain threshold, there is a transition to a lower resistance state, while the initial high conductance resistance can be recovered by a reverse scan.

The spectrum of Figure 4a traces an arc in the fourth quadrant related to the action of the positive inductor element. This feature is very characteristic of lead halide perovskite solar cell impedance results and has been reported in many publications.[62,63] The impedance patterns for a metal halide perovskite memristor around the transition state are shown in Figure 8 (right).[33] Before the onset of the high conduction state, the impedance plot displays the two typical *RC* arcs of the perovskite solar cells.[64] Near the threshold voltage, the memristive behavior dominates the impedance and the former low frequency arc is transformed to the arc in the fourth quadrant by the action of the inductive element, which is associated with the effect of vacancies arriving on the electrode surface.[54]

It is interesting that the inductor features shown in Figures 4 and 8 are not related to any magnetic properties. The behavior of Figure 4a appears in a general type of internal relaxation model, in which the externally measured variable is coupled to a state variable, which relaxes to a pseudoequilibrium state

https://doi.org/10.1021/acs.jpcb.1c03905
J. Phys. Chem. B XXXX, XXX, XXX–XXX

determined by the external variable. The first analysis of the relaxation impedance is due to Göhr and Schiller in a model for electrochemical reaction in which the rate constant k obeys a relaxation equation.[67]

A recent model was described in ref 68 to explain the inductive behavior of lead halide perovskites.[62,63,69,70] In that model, the external voltage V applied to the solar cell reaches equilibrium influenced by the relaxation of an internal surface voltage that is slowed down by ionic motion. It generates an EC including the RL branch of Figure 3. This model gives important insights into the hysteresis of current−voltage curves observed in perovskite solar cells.[71,72] In this system the inductor branch is associated with deleterious surface recombination that becomes active at low frequency, reducing the efficiency of the solar cell.[63] Additional examples of the general EC with inductor associated with interfacial electronic phenomena are sown in Figure 9 for the measurements of an

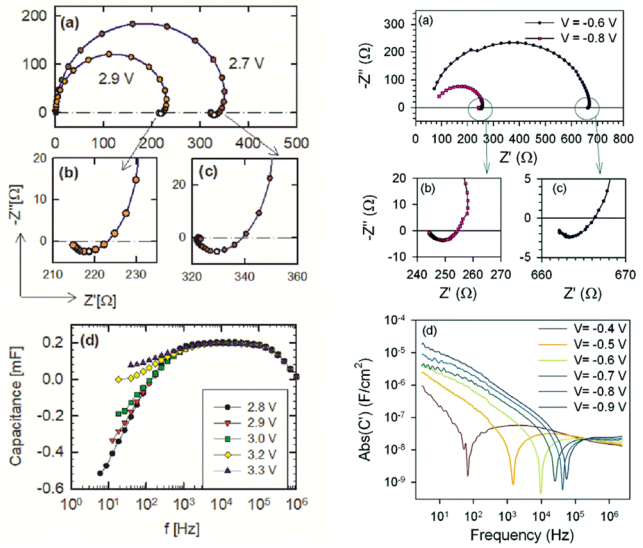

Figure 9. (Left column) Results of the measurement of an ITO/PEDOT/superyellow/Ba/Al organic LED device. (a) Impedance plots for different bias voltages. (b and c) Magnification of the observed inductive behavior at 2.9 and 2.7 V, respectively. (d) Capacitance versus frequency for various bias voltages indicating a region of negative capacitance. Reproduced from ref 65. (Right column) Impedance spectra for a CdS/CdTe solar cell. (a−c) Complex plane plot of the impedance at two different forward biases in the dark. The frequency range employed in the measurement was 1 MHz to 0.1 Hz. (d) Absolute value of capacitance vs frequency at forward bias. Reproduced from ref 66.

OLED device[65] and a CdS/CdTe solar cell.[66] The inductive loop is also observed in a variety of material platforms that have the common property of a memory effect in current−potential curves due to internal ion motion, associated with polarization within the film, e.g., metal oxides[73] and $LiNbO_2$ memristors.[74]

The denomination of negative capacitance requires clarification since it is a general feature that is widely observed in emerging solar cells and other electronic devices.[62,63,66,72] The responses of Figure 4 and the experimental observations in Figures 8 and 9 contain a positive inductor, not a negative capacitor. However, in the impedance analysis it is useful to plot the capacitance (eq 2) vs the frequency, according to the above definitions $C'(\omega) = Re[1/i\omega Z(\omega)]$, as shown in Figure 9. In this plot, the positive inductor RL line certainly displays a negative capacitance effect, Figure 9d, which is the reason for the denomination of negative capacitance.

On the other hand, the memristors are often associated with a negative resistance.[60] The analysis of Figure 4 is restricted to positive circuit elements, while the effect of an NDR will be discussed below in relation to the neuron models.

3.4. Capacitive Memristor. The EC in Figure 3 is quite general based on a broad definition of kinetic equations in the time domain, but it is not the only possible dynamic behavior of a memristor in the frequency domain. In fact, there are a variety of mechanisms under the denomination of memristive devices that require different characterization techniques.[40,75]

We analyze the famous HP titanium dioxide memristor,[39,40] where the memristive property is the variation of dopant concentration in a semiconductor film. The model is defined by the following equations including materials constants R_{on}, R_{off}, D, and μ

$$u = R_0(w)I \tag{20}$$

$$R_0(w) = (R_{on} - R_{off})\frac{w}{D} + R_{off} \tag{21}$$

$$\frac{dw}{dt} = \mu\frac{R_{on}}{D}I \tag{22}$$

Equation 21 defines the function $G(w) = R_0^{-1}$ in eq 8. For the small signal ac perturbation, we obtain eq 10 and

$$s\tilde{w} = \mu\frac{R_{on}}{D}\tilde{I} \tag{23}$$

Therefore, the impedance is

$$Z(\omega) = R_0 + \frac{1}{C_1 s} \tag{24}$$

where the capacitor has the value

$$C_1 = \frac{D}{\bar{I}G_w\mu R_{on}} \tag{25}$$

The EC is shown in Figure 7C. The difference with respect to initial model B is that the relaxation of the internal variable in eq 22 depends on current rather than on voltage, which causes a capacitive rather than an inductive response for the internal variable. Therefore, there is a contrast between voltage- and current-controlled memristors according to the fundamental EC response. At the present time, the generality of such a classification is not known, and it appears to be an important topic for future investigations.

4. ADAPTATIVE EXPONENTIAL INTEGRATE AND FIRE MODEL

4.1. Kinetic Model. In the integrate-and-fire models, the membrane capacitor of the neuron is charged by an external stimulus. When the voltage reaches a certain threshold, the capacitor is discharged, producing an action potential and then the voltage is reset to the rest value.

This type of model has the advantage that it can be solved mathematically, and it has been used to analyze the emergent states in networks of neurons. The simplest model is formed by charging an RC circuit and the subsequent voltage reset. The dynamics can be enriched by features approaching the more complete multichannel Hodgkin−Huxley model, which will be discussed in the next section. In particular, an action potential

https://doi.org/10.1021/acs.jpcb.1c03905
J. Phys. Chem. B XXXX, XXX, XXX−XXX

produces a refractory period in which the neuron cannot be stimulated. These delays influence the neuron firing patterns. They can be described by an adaptation current that is fed back to the voltage with time constant τ_k and a resistance R_a.[12] These models can successfully emulate the spatiotemporal integration of input signals and the firing functions of biological neurons.

Here we analyze the impedance response of the integrate-and-fire adaptative exponential model (AdEx)[76−82] that is able to reproduce many electrophysiological features seen in real neurons with a few parameters that have a physiological interpretation. This model neuron has been realized using perovskite memristors.[37]

The voltage in the membrane u changes with time by a conductance function $f(u)$, a resistor R_I, and a response time τ_m, with the charging capacitance in eq 18. The current I is coupled to an internal adaptation current w that is driven by the departure from the rest potential u_{rest}. The model equations are

$$\tau_m \frac{du}{dt} = f(u) - R_I w + R_I I(t) \tag{26}$$

$$\tau_k \frac{dw}{dt} = \frac{1}{R_a}(u - u_{rest}) - w \tag{27}$$

The model consists of a dynamic system formed by two equations with the general structure of the memristor in eqs 16 and 17. It also belongs to the class of fast-slow dynamical systems. The slow adaptation current is the state variable of the memristor. On the other hand, eqs 26 and 27 have a direct relation to a number of models for bursting oscillations in electrochemical cells.[83,84]

The function $f(u)$ can be found experimentally from the measurement of neuron discharges.[12] It is $f(u_{rest}) = 0$ and increases rapidly after a threshold voltage θ_{th} that launches an action potential. In particular, the AdEx integrate-and-fire model uses the expression[85] shown in Figure 10a

$$f(u) = -(u - u_{rest}) + \Delta_T \exp\left(\frac{u - \theta_{th}}{\Delta_T}\right) \tag{28}$$

where Δ_T is a sharpness parameter. The exponential term approximates the operation of sodium channel, which launches the action potential. The model is composed of two currents in parallel, the passive current associated with the function $f(u)$, and the adaptation current w. Equations 26 and 28 establish the subthreshold dynamics of the model. Once the vertical voltage rise is achieved, the spike is obtained by a reset of the voltage $u \to u_{rest}$ and an increase of the adaptation current $w \to w + b$.

The fixed points are obtained by setting time derivatives $\dot{u} = 0$ and $\dot{w} = 0$ at an external current I_0. The steady-state current−voltage corresponds to the set of fixed points:

$$I_0 = \left(\frac{1}{R_a} + \frac{1}{R_I}\right)(u - u_{rest}) - \frac{\Delta_T}{R_I} \exp\left(\frac{u - \theta_{th}}{\Delta_T}\right) \tag{29}$$

The result is shown in Figure 10b. The plot displays a clear NDR feature at $u > \theta_{th}$, corresponding to the initiation of the neuron spike.

4.2. Impedance Response. We now calculate the ac impedance response. The small perturbation of eqs 26 and 27 at a voltage point $\bar{u}$ gives the equations

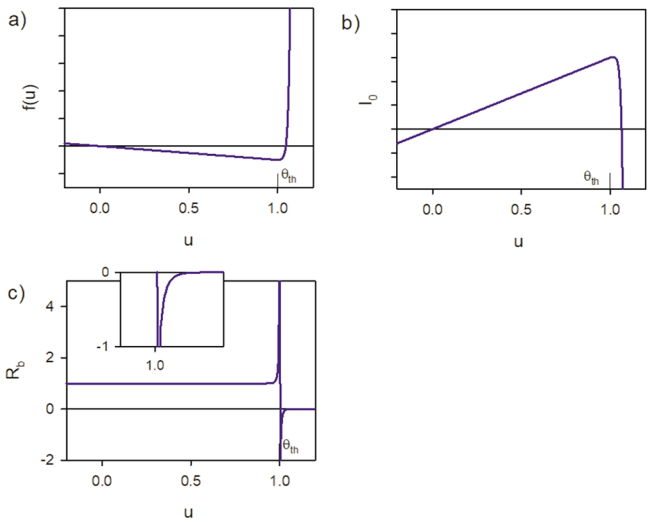

Figure 10. Voltage dependence of quantities in the AdEx model with $u_{rest} = 0$. (a) Function $f(u)$. (b) Stationary current−voltage curve. (c) Resistance R_b; the inset shows the negative values at $u > \theta_{th}$.

$$\tau_m s\tilde{u} = f'\tilde{u} - R_I\tilde{w} + R_I\tilde{I} \tag{30}$$

$$\tau_k s\tilde{w} = \frac{1}{R_a}\tilde{u} - \tilde{w} \tag{31}$$

where

$$f'(\bar{u}) = -1 + \exp\left(\frac{\bar{u} - \theta_{th}}{\Delta_T}\right) \tag{32}$$

The solution to the impedance is given in eq 19. The EC parameters have the values

$$R_b(\bar{u}) = -\frac{R_I}{f'} = \frac{R_I}{1 - \exp\left(\frac{\bar{u} - \theta_{th}}{\Delta_T}\right)} \tag{33}$$

$$L_a = R_a\tau_k \tag{34}$$

Importantly, according to eq 33, the resistance R_b makes a transition from positive to negative values close to $u = \theta_{th}$, which originates from the NDR in Figure 10c.

The fixed points of the system are given in eq 29. To study their stability, we calculate the Jacobian matrix for a small perturbation around the fixed point at $\bar{u}$:

$$\begin{pmatrix} f'/\tau_m & -R_I/\tau_m \\ 1/(R_a\tau_k) & -1/\tau_k \end{pmatrix} \tag{35}$$

Obtaining the eigenvectors, we find the two necessary and sufficient conditions for stability

$$\lambda_+ + \lambda_- = -\frac{1}{R_b C_m} - \frac{R_a}{L_a} < 0 \tag{36}$$

and

$$\lambda_+\lambda_- = \frac{R_a}{L_a C_m}\frac{1}{R_{dc}} > 0 \tag{37}$$

These can also be expressed, respectively, as

$$\frac{\tau_m}{\tau_k} > f'(\bar{u}) \tag{38}$$

https://doi.org/10.1021/acs.jpcb.1c03905
J. Phys. Chem. B XXXX, XXX, XXX−XXX

$$\frac{R_I}{R_a} > f'(\bar{u}) \tag{39}$$

The low-frequency dc resistance is

$$R_{dc} = \left(\frac{1}{R_a} + \frac{1}{R_b}\right)^{-1} \tag{40}$$

The second condition of stability (eq 39) corresponds to

$$R_{dc} > 0 \tag{41}$$

The impedance model corresponds to the EC in Figure 3. Since $f' = -1$ for most of the subthreshold region, the stability is warranted by eqs 38 and 39 and the impedance spectra correspond to those in Figure 4.

Let us analyze in more detail the inductive feature in Figure 4a. The resistance at the intercept $Z'' = 0$ has the value

$$R_{Z''=0} = \frac{R_b}{1 + R_a R_b C_m / L_a} = \frac{R_b}{1 + \frac{R_b}{R_I}\frac{\tau_m}{\tau_k}} \tag{42}$$

The spectrum in Figure 4a reflects the two-step relaxation in the model. Normally, u is the fast variable and w shows a slow relaxation associated with the memory effect. Then, assuming $\tau_m \ll \tau_k$, the impedance response of the system shows a fast relaxation in the high-frequency arc and the real part of the impedance reaches R_b. Then, the slow variable sets in and reduces the dc resistance to the lower R_{dc} value, as commented on previously. More rigorously, the condition in which $R_{Z''=0} > R_{dc}$ is given by

$$\frac{R_I}{R_a} > \frac{\tau_m}{\tau_k} \tag{43}$$

which corresponds to the condition expressed in Figure 4 for the AdExp model specifically. This expression indicates the transition from Figure 4a to Figure 4b when the negative capacitance feature in the fourth quadrant disappears. The condition (eq 43) also indicates the appearance of a Hopf bifurcation when the current is increased, whereas in the opposite case the system undergoes a saddle-node bifurcation.[77] The impedance spectra in the transition zone are shown in the experimental examples of Figure 9. The impedance model parameters and stability conditions are summarized in the Supporting Information.

4.3. Impedance Spectra for Negative Resistance Values. The classification of characteristic impedance spectra for negative R_b is shown in Figure 5. The condition in eq 43 also indicates which condition of stability (eqs 38 or 39) is broken first. If eq 43 is satisfied, then there is a region where the two parallel currents compete, with R_b being negative and R_{dc} still being positive, in the potential range determined by the condition

$$\frac{R_I}{R_a} > f'(\bar{u}) = -\frac{R_I}{R_b} > \frac{\tau_m}{\tau_k} \tag{44}$$

This region produces the impedance pattern of Figure 5 defined before as a "hidden negative impedance".[31] Here the complex $Z(\omega)$ encircles the origin, and the imaginary part of the impedance has a zero value at a finite frequency of the negative real part. This is a signal of the Hopf instability, as mentioned earlier.

Figure 5 shows the impedance spectra in the presence of a true NDR. These patterns are well documented in the literature of electrochemical oscillations, in the case of oscillations induced by a Hopf bifurcation under potentiostatic control.[86,87] Different examples of the spectra for formaldehyde oxidation are shown in Figure 11. These impedance patterns are also very typical for electrochemical passivation and corrosion.[88,89]

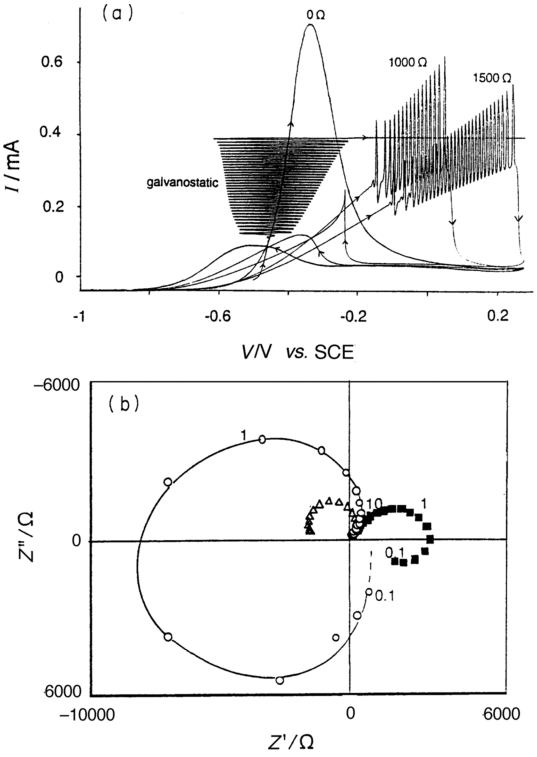

Figure 11. (a) Voltammogram of 0.1 M HCHO in 0.1 M NaOH for 0, 1000, and 1500 Ω external resistance (internal cell resistance ca. 95 Ω). Scan rate 10 mV s^{-1}, 3000 rpm. Amperogram taken at 0.01 mA s^{-1}. (b) Impedance diagrams taken at −0.50 V (■), −0.45 V (○), and −0.35 V (Δ). Indicated frequencies are in Hz. Reproduced from ref 87.

Figure 12 indicates the impedance spectrum when the RL elements are both negative. This is not a case that emanates from the AdEx model, but it is also interesting since it occurs naturally in the sodium channel of the Hodgkin−Huxley model discussed below.

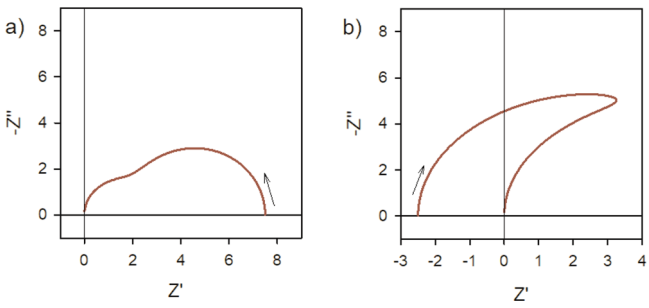

Figure 12. Complex plane impedance spectra of the AdEx model, $R_a < 0$ and $L_a < 0$. (a) $R_I = 1$, $R_a = -5$, $R_b = 3$, $R_{dc} = 7.5$, $\tau_m = 10$, $\tau_k = 100$, and $L_a = -500$. (b) $R_I = 10$, $R_a = -2$, $R_b = 10$, $R_{dc} = -2.5$, $\tau_m = 10$, $\tau_k = 100$, and $L_a = -200$. The arrow indicates the direction of increasing frequency.

https://doi.org/10.1021/acs.jpcb.1c03905
J. Phys. Chem. B XXXX, XXX, XXX−XXX

The transient response to a current step in the time domain is represented in Figure 13. Figure 13a shows a damped oscillation, while Figure 13b corresponding to the hidden negative resistance shows a periodic amplification corresponding to negative damping.

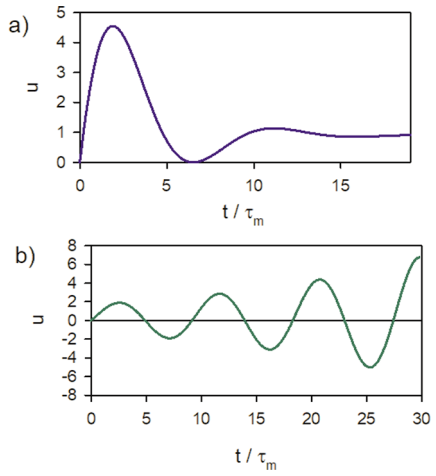

Figure 13. Transient voltage in the AdEx model after a small perturbation constant current onset at $t = 0$. (a) $R_I = 5$, $R_a = 1$, $R_b = 10$, $\tau_m = 10$, andn $\tau_k = 100$. (b) $R_I = 1$, $R_a = 0.2$, $R_b = -5$, $R_{dc} = 0.2083$, $\tau_m = 10$, and $\tau_k = 100$.

A complete study of the oscillations, spiking dynamics, and bifurcations of the AdEx model depending on the external current I is presented by Touboul et al.[77]

5. HODGKIN–HUXLEY SQUID GIANT AXON MODEL

5.1. Kinetic Model. Finally, we aim to calculate the impedance response from the Hodgkin–Huxley dynamic model for the squid giant axon membrane.[11] This is a landmark model that is extremely accurate for describing neuron dynamics. A development of the small perturbation ac model was presented by Chua and co-workers in order to investigate the stability conditions.[35,36] Here, we aim to understand the main impedance responses and provide an interpretation based on the simpler models that have been analyzed earlier in this article, namely, the memristor and the adaptative integrate-and-fire neuron.

The original H–H model follows different current and voltage references from those usually adopted in the literature.[90,91] Therefore, we rewrite the H–H equations such that they comply with this convention, i.e., current direction from inside to outside the membrane and voltage polarity positive inside and negative outside, as shown in Figure 14a. Moreover, we consider the membrane potential as it is, and we do not use the original transformation, where the origin is taken at the resting potential of the membrane ($V_M = V_r$).

The electrical circuit of the membrane, shown in Figure 14a, has four different branches that correspond to the membrane capacitance, the potassium ion channel, the sodium ion channel, and the leakage current, respectively. As noted in Figure 14a, the resistances across the potassium (R_K) and sodium (R_{Na}) channels are not constant, but they depend both on time and voltage, reflecting the complex dynamics in response to external inputs. The model provides complete kinetic equations for the different channels; therefore, we will

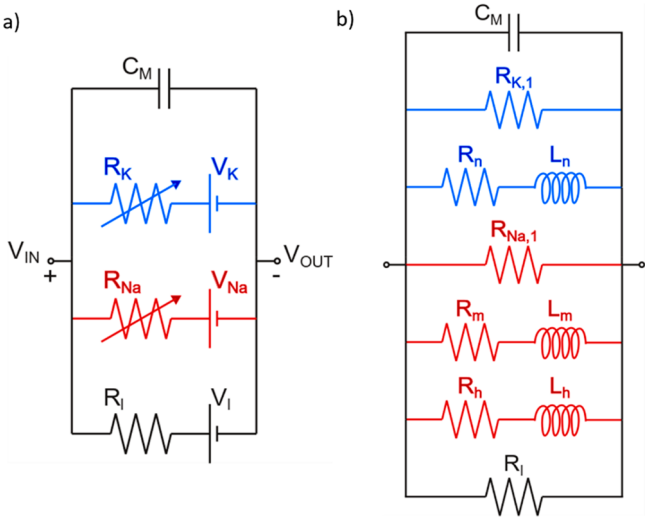

Figure 14. (a) Hodgkin–Huxley electrical model for the squid giant axon membrane consisting of variable resistances in the ion channels as defined in the original publication. (b) Equivalent circuit for the Hodgkin–Huxley model for small ac voltage perturbations. The potassium channel components are indicated in blue, and the sodium elements, in red.

be able to develop the small ac EC elements at a fixed point, using the same method applied in the previous examples. Our goal is to derive a small perturbation EC in which the elements depend on voltage but are *time-independent*, and the result is shown in Figure 14b.

The current through the membrane can be written as the addition of the four contributions in Figure 14a

$$I_M = I_C + I_K + I_{Na} + I_l \tag{45}$$

The currents obey the expressions

$$I_C = C_M \frac{dV_M}{dt} \tag{46}$$

$$I_K = \frac{1}{R_K}(V_M - V_K) \tag{47}$$

$$I_{Na} = \frac{1}{R_{Na}}(V_M - V_{Na}) \tag{48}$$

$$I_l = \frac{1}{R_l}(V_M - V_l) \tag{49}$$

Here, the membrane voltage V_M is defined as

$$V_M = V_{in} - V_{out} \tag{50}$$

and the other voltages follow the polarity indicated in Figure 14a and have values of $V_K = -77$ mV, $V_{Na} = 50$ mV, and $V_l = -54.387$ mV. Each of these voltages relate to the membrane voltages that cancel the current in each channel. We consider a resting potential of $V_r = -65$ mV, which corresponds to the resting potential at a temperature of $T = 6.3$ °C.[11] The resting potential is the voltage at which there is no current through the membrane. The membrane capacitance C_M has a value of 1 μF cm^{-2}, and the leakage resistance is 3.33 kΩ cm^2.

The potassium resistance is described by the following expression

https://doi.org/10.1021/acs.jpcb.1c03905
J. Phys. Chem. B XXXX, XXX, XXX–XXX

$$\frac{1}{R_K} = \frac{1}{R_{K0}} n^4 \tag{51}$$

where R_{K0} = 27.78 Ω cm^2 is the minimum value of the resistance and n is a dimensionless potassium gate-activation variable that takes values from 0 to 1 and satisfies the following equation:

$$\frac{dn}{dt} = \alpha_n(1 - n) - \beta_n n \tag{52}$$

Here, the transfer rate coefficients α_n and β_n are time-independent and voltage-dependent by

$$\alpha_n = \frac{0.01(10 - V')}{e^{10-V'/10} - 1} \tag{53}$$

$$\beta_n = \frac{0.125}{e^{V'/80}} \tag{54}$$

where α_n and β_n are in ms $^{-1}$ and $V' = V_M - V_r$ is in mV.

The sodium resistance is described by a similar expression:

$$\frac{1}{R_{Na}} = \frac{1}{R_{Na0}} m^3 h \tag{55}$$

In the same way as before, R_{Na0} = 8.33 Ω cm^2 is the minimum value of the sodium resistance. However, the sodium channel has two gate-activation variables m and h. They are both dimensionless and take values from 0 to 1, and similar to the variable n, they are described by the equations

$$\frac{dm}{dt} = \alpha_m(1 - m) - \beta_m m \tag{56}$$

$$\frac{dh}{dt} = \alpha_h(1 - h) - \beta_h h \tag{57}$$

Again, α_m and β_m are time-independent and voltage-dependent. Their voltage dependence is given by

$$\alpha_m = \frac{0.1(25 - V')}{e^{25-V'/10} - 1} \tag{58}$$

$$\beta_m = \frac{4}{e^{V'/18}} \tag{59}$$

α_h and β_h are also voltage-dependent, according to the equations

$$\alpha_h = \frac{0.07}{e^{V'/20}} \tag{60}$$

$$\beta_h = \frac{1}{e^{30-V'/10} + 1} \tag{61}$$

All of the transfer rate coefficients are in ms $^{-1}$, and $V' = V_M - V_r$ is in mV.

We can rewrite eqs 47 and 48 of the currents across the two ion channels as

$$I_K = \frac{1}{R_{K0}} n^4 (V_M - V_K) \tag{62}$$

$$I_{Na} = \frac{1}{R_{Na0}} m^3 h (V_M - V_{Na}) \tag{63}$$

5.2. Impedance Response. From these equations, we can calculate the ac impedance response of the H−H model across each branch. The small perturbation and Laplace transform of eqs 46, 62, 63, and 49 give the equations

$$\tilde{I}_C = sC_M \tilde{V}_M \tag{64}$$

$$\tilde{I}_K = \frac{1}{R_{K0}} 4\bar{n}^3 (\bar{V}_M - V_K)\tilde{n} + \frac{1}{R_{K0}} \bar{n}^4 \tilde{V}_M \tag{65}$$

$$\tilde{I}_{Na} = \frac{1}{R_{Na0}} 3\bar{m}^2 \bar{h} (\bar{V}_M - V_{Na})\tilde{m} + \frac{1}{R_{Na0}} \bar{m}^3 (\bar{V}_M - V_{Na})\tilde{h} + \frac{1}{R_{Na0}} \bar{m}^3 \bar{h} \tilde{V}_M \tag{66}$$

$$\tilde{I}_l = \frac{1}{R_l} \tilde{V}_M \tag{67}$$

Here, in eqs 65 and 66, perturbed variables $\tilde{n}$, $\tilde{m}$, and $\tilde{h}$ appear. We can calculate them from the small perturbation and Laplace transform from eqs 52, 56, and 57:

$$s\tilde{n} = \left[\frac{\partial \bar{\alpha}_n}{\partial V_M}(1 - \bar{n}) - \frac{\partial \bar{\beta}_n}{\partial V_M}\bar{n}\right]\tilde{V}_M - (\bar{\alpha}_n + \bar{\beta}_n)\tilde{n} \tag{68}$$

$$s\tilde{m} = \left[\frac{\partial \bar{\alpha}_m}{\partial V_M}(1 - \bar{m}) - \frac{\partial \bar{\beta}_m}{\partial V_M}\bar{m}\right]\tilde{V}_M - (\bar{\alpha}_m + \bar{\beta}_m)\tilde{m} \tag{69}$$

$$s\tilde{h} = \left[\frac{\partial \bar{\alpha}_h}{\partial V_M}(1 - \bar{h}) - \frac{\partial \bar{\beta}_h}{\partial V_M}\bar{h}\right]\tilde{V}_M - (\bar{\alpha}_h + \bar{\beta}_h)\tilde{h} \tag{70}$$

From the combination of eqs 64−70, we derive the impedance given by

$$Z = \frac{\tilde{V}_M}{\tilde{I}_M} = \frac{\tilde{V}_M}{\tilde{I}_C + \tilde{I}_K + \tilde{I}_{Na} + \tilde{I}_l} \tag{71}$$

Rearranging all of the terms obtained, we can get an expression for impedance with the following elements:

$$Z = \frac{\tilde{V}_M}{\tilde{I}_M} = \left[sC_M + \frac{1}{R_{K,1}} + \frac{1}{R_n + sL_n} + \frac{1}{R_{Na,1}} + \frac{1}{R_m + sL_m} + \frac{1}{R_h + sL_h} + \frac{1}{R_l}\right]^{-1} \tag{72}$$

The EC generated by this impedance is shown in Figure 14b, and the values of the voltage-dependent elements are detailed as follows:

$$R_{K,1}(\bar{V}_M) = \frac{R_{K0}}{\bar{n}^4} \tag{73}$$

$$R_n(\bar{V}_M) = \frac{R_{K0}}{4\bar{n}^3(\bar{V}_M - V_K)\tau_n\left[\frac{\partial \bar{\alpha}_n}{\partial V_M}(1 - \bar{n}) - \frac{\partial \bar{\beta}_n}{\partial V_M}\bar{n}\right]} \tag{74}$$

$$L_n(\bar{V}_M) = R_n \tau_n \tag{75}$$

$$R_{Na,1}(\bar{V}_M) = \frac{R_{Na0}}{\bar{m}^3 \bar{h}} \tag{76}$$

https://doi.org/10.1021/acs.jpcb.1c03905
J. Phys. Chem. B XXXX, XXX, XXX−XXX

$$R_m(\bar{V}_M) = \frac{R_{Na0}}{3\bar{m}^2\bar{h}(\bar{V}_M - V_{Na})\tau_m\left[\frac{\partial\bar{\alpha}_m}{\partial V_M}(1-\bar{m}) - \frac{\partial\bar{\beta}_m}{\partial V_M}\bar{m}\right]} \quad (77)$$

$$L_m(\bar{V}_M) = R_m\tau_m \quad (78)$$

$$R_h(\bar{V}_M) = \frac{R_{Na0}}{\bar{m}^3(\bar{V}_M - V_{Na})\tau_h\left[\frac{\partial\bar{\alpha}_h}{\partial V_M}(1-\bar{h}) - \frac{\partial\bar{\beta}_h}{\partial V_M}\bar{h}\right]} \quad (79)$$

$$L_h(\bar{V}_M) = R_h\tau_h \quad (80)$$

The different relaxation time constants τ_i of each activation-gate variable are defined as

$$\tau_i = \frac{1}{\alpha_i + \beta_i} \quad (81)$$

These results correspond to those obtained by Chua et al.[35] with a different voltage reference.

5.3. Interpretation of the Impedance Spectra. We aim to analyze impedance spectra in the region where the real part of the impedance takes negative values, since this is the requirement for inducing oscillations and spiking. This occurs between $V_M = -42.99$ mV and $V_M = -60.25$ mV. In Figure 15,

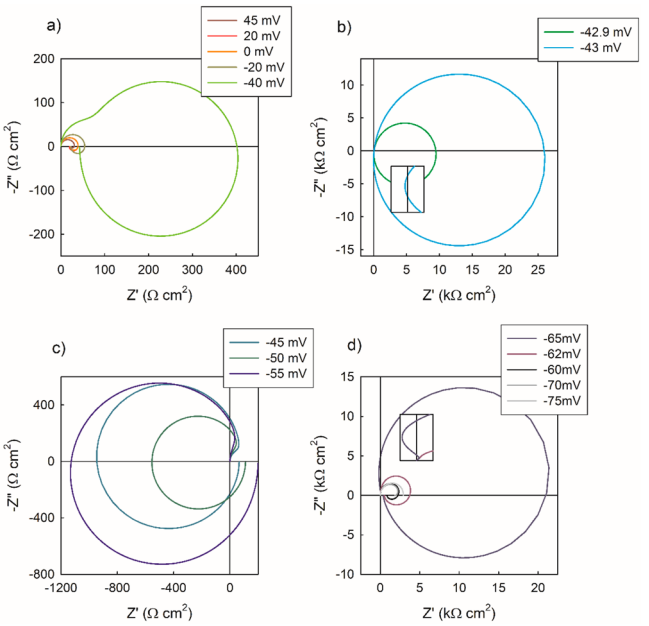

Figure 15. Impedance complex plane plots for voltages (a) above the upper limit of the negative impedance region, (b) around the upper limit $V_M = -42.99$ mV, (c) in the negative impedance region, and (d) around the lower limit $V_M = -60.25$ mV.

we show a set of impedance complex plots of the full model of Figure 14b for representative voltage values above this range (Figure 15a,b), in this range (Figure 15b,c,d) and below it (Figure 15d).

The negative value of the real part of the impedance is clearly observed at frequencies different from zero, it is therefore a "hidden negative impedance". The values close to the voltage range limit have only a small region in the negative area, while the intermediate values have most of the spectrum at the negative part, Figure 15c.

To better understand the EC and the wide diversity of characteristic impedance spectra obtained for the Hodgkin–Huxley model and compare it with other systems with similar ECs, we now analyze the impedance response of the individual K and Na channels that compose the model.

We first look at the spectra generated by the potassium channel with the constant elements C_M and R_l. The partial EC is represented in Figure 16a, and it is equivalent to the general

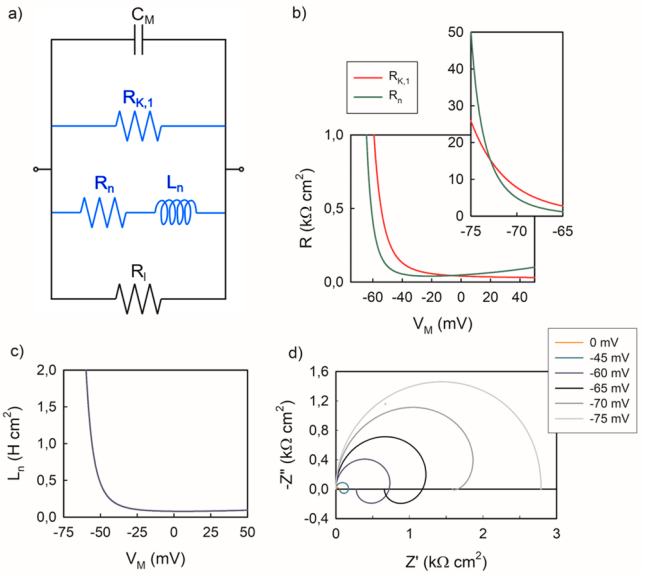

Figure 16. Impedance details of the K channel. (a) EC used for (d). (b and c) Values of the elements for the range of membrane voltages. (d) Impedance complex plane plot for different values.

memristor EC previously presented in Figure 3. Figure 16b,c shows the values of the circuit elements generated by the potassium channel for the voltage range spanning V_K to V_{Na}. The graphs show that the resistances have relatively low values compared to the leakage resistance (3.33 kΩ) for voltages above the resting potential V_r. Below this value, both resistances start to increase until they take huge values. The same happens in the case of the inductor in Figure 16c.

In Figure 16d, we can see the impedance complex plane plots for a variety of membrane voltages. The spectra generated by this circuit and the evolution of these elements generally show an arc at the first quadrant at high frequency and another arc in the fourth quadrant at low frequency. This behavior has been described above in Figure 4. The arcs are relatively small at voltages above $V_M = -20$ mV, where the values of all of the potassium channel resistances and inductor are small. Below these values, the arcs start to increase until the fourth quadrant arc disappears, and the spectrum is dominated by the constant elements. This means that the potassium channel closes as we get closer to voltage V_K.

If we calculate the Jacobian and apply the stability conditions in the same way that we did before but for this EC, we get the following conditions:

$$-\left(\frac{1}{R_{k,1}} + \frac{1}{R_l}\right) < \frac{C_M}{\tau_n} \quad (82)$$

https://doi.org/10.1021/acs.jpcb.1c03905
J. Phys. Chem. B XXXX, XXX, XXX−XXX

$$-\left(\frac{1}{R_{k,1}}+\frac{1}{R_l}\right)<\frac{1}{R_n} \tag{83}$$

Moreover, if we apply the condition $R_{Z''=0} > R_{dc}$ for the appearance of inductive loops, then we get

$$-\left(\frac{1}{R_{k,1}}+\frac{1}{R_l}\right)<\frac{C_M}{\tau_n}<\frac{1}{R_n} \tag{84}$$

Since the values of all of these elements and parameters are fixed for any given membrane voltage, we can predict the appearance of the inductive loops as well as the stable voltage values. For this aim, we plot the three factors in Figure 17 to find those voltages. In this figure, we have defined the resistance $R_c^{-1} = R_{k,1}^{-1} + R_l^{-1}$.

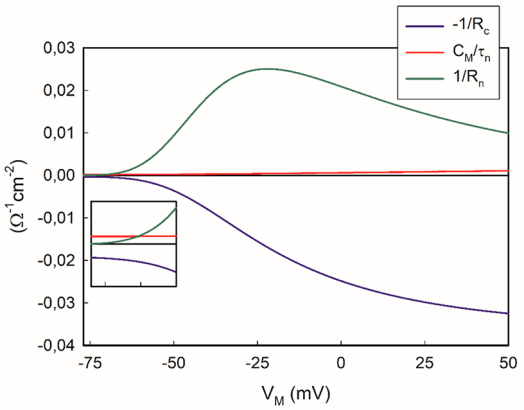

Figure 17. Factors for the conditions of stability and appearance of inductive loops.

From Figure 17, we can conclude that the potassium channel circuit is stable in the whole range of voltages. Moreover, we see a wide range of voltages in which the inductive loop will appear, and we can estimate the voltage where it disappears. This is below a voltage around $V_M = -70$ mV, which agrees with the spectra plotted in Figure 16d.

Looking at the sodium channel, we build in Figure 18a a partial EC including the elements of the membrane; therefore, we can again see when the channel closes and these elements dominate. As we can see, this channel is richer in the number of elements. From Figure 18b,c, we find elements that take negative values. These are the elements R_m and L_m, and they make the spectra generated from this channel even richer, with spectra appearing in any of the four quadrants of the complex plane representation, as previously demonstrated in section 2.3.

As in the case of the potassium channel, the elements have low values in a certain range of voltages, while they take huge values outside this range. This is clearly seen in Figure 18b,c, and it relates to the fact that at voltages 20 mV < V_M < −65 mV the sodium channel is mainly closed, and we again see a single arc corresponding to the constant membrane elements in Figure 19. However, inside this range we again see the memristive inductive loop into the fourth quadrant at V_M = −20 mV. More interestingly, we see the hidden negative resistance at V_M = −30 mV and a clear negative resistance from approximately V_M = −40 to −65 mV. Therefore, it is evident that the channel causing the negative impedance in the whole

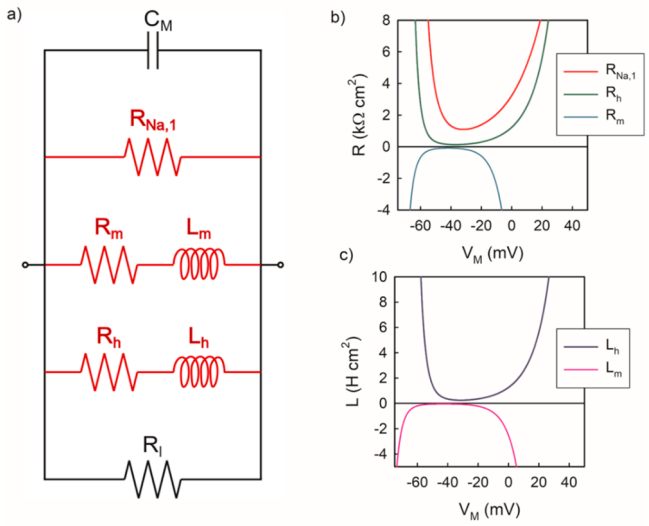

Figure 18. Impedance details of the Na channel. (a) EC used for the Na channel. (b and c) Values of the resistances and inductors for the range of membrane voltages, respectively.

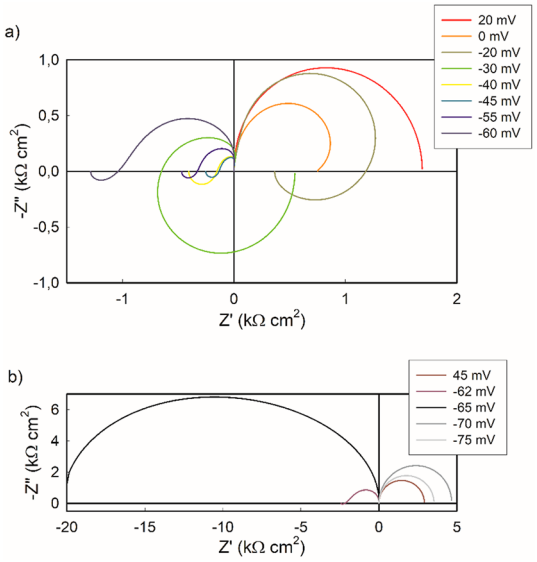

Figure 19. Impedance complex plane plots for the sodium channel EC. Spectra with (a) smaller and (b) larger impedance values.

membrane is the sodium channel. However, the full membrane will not show a negative impedance at zero frequency.

6. CONCLUSIONS

The method we have developed in this article consists of the determination of the small perturbation ac IS response of highly nonlinear systems, related to memristors and the neuromorphic response, starting from the time domain constitutive equations of each model. We showed the connection of the impedance response and the shape of the spectra to the physical interpretation of memory effects and stability, following previous insights in fast-slow dynamical systems, stability theory, and electrochemical oscillations.

First, we presented a frequency domain analysis of memristors. We showed that the memristor can be decomposed into a simple equivalent circuit and that it cannot be regarded as an additional fundamental element for a small

https://doi.org/10.1021/acs.jpcb.1c03905
J. Phys. Chem. B XXXX, XXX, XXX−XXX

signal response. This is because the mechanism of memory is well represented by a resistor-inductor line. The basic structure of the impedance model is obtained across different material platforms and independent fields of study. There is possibly a universal behavior related to the suggested kinetic memory effect that needs further investigation. Nevertheless, the model is not unique to describing memristor systems. There is indeed a very broad type of responses under the label of memristive systems based on different mechanisms and physical effects.

The impedance response of the adaptative exponential integrate-and-fire model for the neuron membrane is similar to that of the memristor, thus confirming them as good candidates for neuromorphic computations. We have made a classification of the spectra generated by this model, and we have established the required conditions for the stability of the impedance response. A variety of criteria consisting of relations among the model parameters have been given in order to clarify which conditions generate each kind of spectra.

The same has been made for the Hodgkin−Huxley model for the squid giant axon. We made an extended calculation of the full impedance model, showing the full equivalent circuit with time-independent elements that governs the operation of these ion-channeled membranes. We have presented the spectra generated by this model for a wide range of voltages, finding a wide variety of shapes, including the hidden negative resistance. With respect to the previously described simple models, this model has the additional complexity of consisting of different channels that cause positive and negative feedback loops. To obtain better insight into the concerted action that produces the diverse impedance spectra responses, we investigated separately the individual ion channel responses. Interestingly, we found that the potassium channel fulfills the stability conditions over the entire voltage range and that the condition for inductive loops is satisfied. However, the sodium channel is more complex, and its equivalent circuit includes a branch with negative elements (a resistance and an inductor) that produce all kind of spectra going through the four quadrants. This feature is responsible for the positive feedback that causes depolarization, including the hidden negative resistance in the full model.

In summary, we have suggested a method to analyze the response of a required complex fast-slow dynamical system in the frequency domain as a tool for constructing material systems with similar functionality.

■ ASSOCIATED CONTENT

Supporting Information

The Supporting Information is available free of charge at https://pubs.acs.org/doi/10.1021/acs.jpcb.1c03905.

Elements of the equivalent circuit for each model, equivalent circuit parameters, and conditions of the equivalent circuit elements (PDF)

■ AUTHOR INFORMATION

Corresponding Author

Juan Bisquert − *Institute of Advanced Materials (INAM), Universitat Jaume I, 12006 Castelló, Spain;* orcid.org/0000-0003-4987-4887; Email: bisquert@uji.es

Author

Agustín Bou − *Institute of Advanced Materials (INAM), Universitat Jaume I, 12006 Castelló, Spain;* orcid.org/0000-0002-7535-5063

Complete contact information is available at: https://pubs.acs.org/10.1021/acs.jpcb.1c03905

Notes

The authors declare no competing financial interest.

■ ACKNOWLEDGMENTS

We thank Generalitat Valenciana for the project PROMETEO/2020/028. A.B. acknowledges FPI studentship funding from Ministerio de Ciencia e Innovación of Spain (BES-2017-080351).

■ REFERENCES

(1) Basheer, I. A.; Hajmeer, M. Artificial neural networks: fundamentals, computing, design, and application. *J. Microbiol. Methods* **2000**, *43*, 3−31.

(2) Indiveri, G.; Linares-Barranco, B.; Legenstein, R.; Deligeorgis, G.; Prodromakis, T. Integration of nanoscale memristor synapses in neuromorphic computing architectures. *Nanotechnology* **2013**, *24*, 384010.

(3) Tang, J.; Yuan, F.; Shen, X.; Wang, Z.; Rao, M.; He, Y.; Sun, Y.; Li, X.; Zhang, W.; Li, Y.; Gao, B.; Qian, H.; Bi, G.; Song, S.; Yang, J. J.; Wu, H. Bridging Biological and Artificial Neural Networks with Emerging Neuromorphic Devices: Fundamentals, Progress, and Challenges. *Adv. Mater.* **2019**, *31*, 1902761.

(4) Tuchman, Y.; Mangoma, T. N.; Gkoupidenis, P.; van de Burgt, Y.; John, R. A.; Mathews, N.; Shaheen, S. E.; Daly, R.; Malliaras, G. G.; Salleo, A. Organic neuromorphic devices: Past, present, and future challenges. *MRS Bull.* **2020**, *45*, 619−630.

(5) Mehonic, A.; Kenyon, A. J. Emulating the Electrical Activity of the Neuron Using a Silicon Oxide RRAM Cell. *Front. Neurosci.* **2016**, *10*, 10.

(6) Zhang, Y.; Wang, Z.; Zhu, J.; Yang, Y.; Rao, M.; Song, W.; Zhuo, Y.; Zhang, X.; Cui, M.; Shen, L.; Huang, R.; Yang, J. J. Brain-inspired computing with memristors: Challenges in devices, circuits, and systems. *Appl. Phys. Rev.* **2020**, *7*, 011308.

(7) Burr, G. W.; Shelby, R. M.; Sebastian, A.; Kim, S.; Kim, S.; Sidler, S.; Virwani, K.; Ishii, M.; Narayanan, P.; Fumarola, A.; Sanches, L. L.; Boybat, I.; Le Gallo, M.; Moon, K.; Woo, J.; Hwang, H.; Leblebici, Y. Neuromorphic computing using non-volatile memory. *Adv. Phys.: X* **2017**, *2*, 89−124.

(8) Zhang, X.; Zhuo, Y.; Luo, Q.; Wu, Z.; Midya, R.; Wang, Z.; Song, W.; Wang, R.; Upadhyay, N. K.; Fang, Y.; Kiani, F.; Rao, M.; Yang, Y.; Xia, Q.; Liu, Q.; Liu, M.; Yang, J. J. An artificial spiking afferent nerve based on Mott memristors for neurorobotics. *Nat. Commun.* **2020**, *11*, 51.

(9) Zhang, X.; Wang, W.; Liu, Q.; Zhao, X.; Wei, J.; Cao, R.; Yao, Z.; Zhu, X.; Zhang, F.; Lv, H.; Long, S.; Liu, M. An Artificial Neuron Based on a Threshold Switching Memristor. *IEEE Electron Device Lett.* **2018**, *39*, 308−311.

(10) Kim, S.; Roe, D. G.; Choi, Y. Y.; Woo, H.; Park, J.; Lee, J. I.; Choi, Y.; Jo, S. B.; Kang, M. S.; Song, Y. J.; Jeong, S.; Cho, J. H. Artificial stimulus-response system capable of conscious response. *Sci. Adv.* **2021**, *7*, No. eabe3996.

(11) Hodgkin, A. L.; Huxley, A. F. A quantitative description of membrane current and its application to conduction and excitation in nerve. *J. Physiol.* **1952**, *117*, 500−544.

(12) Gerstner, W.; Kistler, W. M.; Naud, R.; Paninski, L. *Neuronal Dynamics: From Single Neurons to Networks and Models of Cognition*; Cambridge University Press, 2014.

(13) Burkitt, A. N. A Review of the Integrate-and-fire Neuron Model: I. Homogeneous Synaptic Input. *Biol. Cybern.* **2006**, *95*, 1−19.

(14) Pickett, M. D.; Medeiros-Ribeiro, G.; Williams, R. S. A scalable neuristor built with Mott memristors. *Nat. Mater.* **2013**, *12*, 114−117.
(15) Bredar, A. R. C.; Chown, A. L.; Burton, A. R.; Farnum, B. H. Electrochemical Impedance Spectroscopy of Metal Oxide Electrodes for Energy Applications. *ACS Appl. Ener. Mater.* **2020**, *3*, 66−98.
(16) von Hauff, E. Impedance Spectroscopy for Emerging Photovoltaics. *J. Phys. Chem. C* **2019**, *123*, 11329−11346.
(17) Fabregat-Santiago, F.; Garcia-Belmonte, G.; Mora-Seró, I.; Bisquert, J. Characterization of nanostructured hybrid and organic solar cells by impedance spectroscopy. *Phys. Chem. Chem. Phys.* **2011**, *13*, 9083−9118.
(18) Lopez-Varo, P.; Jiménez-Tejada, J. A.; García-Rosell, M.; Ravishankar, S.; Garcia-Belmonte, G.; Bisquert, J.; Almora, O. Device Physics of Hybrid Perovskite Solar cells: Theory and Experiment. *Adv. Energy Mater.* **2018**, *8*, 1702772.
(19) Wang, H.; Guerrero, A.; Bou, A.; Al-Mayouf, A. M.; Bisquert, J. Kinetic and material properties of interfaces governing slow response and long timescale phenomena in perovskite solar cells. *Energy Environ. Sci.* **2019**, *12*, 2054−2079.
(20) Johnston, M. B.; Herz, L. M. Hybrid Perovskites for Photovoltaics: Charge-Carrier Recombination, Diffusion, and Radiative Efficiencies. *Acc. Chem. Res.* **2016**, *49*, 146−154.
(21) Grimnes, S.; Martinsen, O. G. *Bioimpedance and Bioelectricity Basics*, 3rd ed.; Academic Press, 2015.
(22) Stupin, D. D.; Kuzina, E. A.; Abelit, A. A.; Emelyanov, A. K.; Nikolaev, D. M.; Ryazantsev, M. N.; Koniakhin, S. V.; Dubina, M. V. Bioimpedance Spectroscopy: Basics and Applications. *ACS Biomater. Sci. Eng.* **2021**, *7*, 1962.
(23) Xu, Y.; Xie, X.; Duan, Y.; Wang, L.; Cheng, Z.; Cheng, J. A review of impedance measurements of whole cells. *Biosens. Bioelectron.* **2016**, *77*, 824−836.
(24) Spencer, D. C.; Paton, T. F.; Mulroney, K. T.; Inglis, T. J. J.; Sutton, J. M.; Morgan, H. A fast impedance-based antimicrobial susceptibility test. *Nat. Commun.* **2020**, *11*, 5328.
(25) Zou, Y.; Guo, Z. A review of electrical impedance techniques for breast cancer detection. *Med. Eng. Phys.* **2003**, *25*, 79−90.
(26) Van Eijnatten, M. A.; Van Rijssel, M. J.; Peters, R. J.; Verdaasdonk, R. M.; Meijer, J. H. Comparison of cardiac time intervals between echocardiography and impedance cardiography at various heart rates. *J. Elec. Bioimped.* **2014**, *5*, 2−8.
(27) Pradhan, R.; Mitra, A. D. S. Quantitative evaluation of blood glucose concentration using impedance sensing devices. *J. Elec. Bioimped.* **2013**, *4*, 73−77.
(28) Vardi, R.; Goldental, A.; Marmari, H.; Brama, H.; Stern, E. A.; Sardi, S.; Sabo, P.; Kanter, I. Neuronal response impedance mechanism implementing cooperative networks with low firing rates and μs precision. *Front. Neural Circuits* **2015**, *9*, DOI: 10.3389/fncir.2015.00029.
(29) Bou, A.; Pockett, A.; Raptis, D.; Watson, T.; Carnie, M. J.; Bisquert, J. Beyond Impedance Spectroscopy of Perovskite Solar Cells: Insights from the Spectral Correlation of the Electrooptical Frequency Techniques. *J. Phys. Chem. Lett.* **2020**, *11*, 8654−8659.
(30) Fletcher, S. Tables of Degenerate Electrical Networks for Use in the Equivalent-Circuit Analysis of Electrochemical Systems. *J. Electrochem. Soc.* **1994**, *141*, 1823−1826.
(31) Koper, M. T. M. Oscillations and Complex Dynamical Bifurcations in Electrochemical Systems. *Adv. Chem. Phys.* **2007**, *92*, 161.
(32) Naito, M.; Tanaka, N.; Okamoto, H. General relationship between complex impedance and linear stability in electrochemical systems. *J. Chem. Phys.* **1999**, *111*, 9908−9917.
(33) Gonzales, C.; Guerrero, A.; Bisquert, J. Spectral properties of the dynamic state transition in metal halide perovskite-based memristor exhibiting negative capacitance. *Appl. Phys. Lett.* **2021**, *118*, 073501.
(34) Koper, M. T. M. Non-linear phenomena in electrochemical systems. *J. Chem. Soc., Faraday Trans.* **1998**, *94*, 1369−1378.
(35) Chua, L.; Sbitnev, V.; Kim, H. Hodgkin-Huxley axon is made of memristors. *Int. J. Bifurcation Chaos Appl. Sci. Eng.* **2012**, *22*, 1230011.
(36) Chua, L.; Sbitnev, V.; Kim, H. Neurons are poised near the edge of chaos. *Int. J. Bifurcation Chaos Appl. Sci. Eng.* **2012**, *22*, 1250098.
(37) Yang, J.-Q.; Wang, R.; Wang, Z.-P.; Ma, Q.-Y.; Mao, J.-Y.; Ren, Y.; Yang, X.; Zhou, Y.; Han, S.-T. Leaky integrate-and-fire neurons based on perovskite memristor for spiking neural networks. *Nano Energy* **2020**, *74*, 104828.
(38) Chua, L. Memristor-The missing circuit element. *IEEE Trans. Circuit Theory* **1971**, *18*, 507−519.
(39) Strukov, D. B.; Snider, G. S.; Stewart, D. R.; Williams, R. S. The missing memristor found. *Nature* **2008**, *453*, 80−83.
(40) Sun, K.; Chen, J.; Yan, X. The Future of Memristors: Materials Engineering and Neural Networks. *Adv. Funct. Mater.* **2021**, *31*, 2006773.
(41) Pershin, Y. V.; Di Ventra, M. Memory effects in complex materials and nanoscale systems. *Adv. Phys.* **2011**, *60*, 145−227.
(42) Linares-Barranco, B.; Serrano-Gotarredona, T. Memristance can explain Spike-Time-Dependent-Plasticity in Neural Synapses. *Nat. Proc.* 2009.
(43) Jo, S. H.; Chang, T.; Ebong, I.; Bhadviya, B. B.; Mazumder, P.; Lu, W. Nanoscale Memristor Device as Synapse in Neuromorphic Systems. *Nano Lett.* **2010**, *10*, 1297−1301.
(44) Prezioso, M.; Mahmoodi, M. R.; Bayat, F. M.; Nili, H.; Kim, H.; Vincent, A.; Strukov, D. B. Spike-timing-dependent plasticity learning of coincidence detection with passively integrated memristive circuits. *Nat. Commun.* **2018**, *9*, 5311.
(45) *Advances in Neuromorphic Memristor Science and Applications*; Kozma, R., Pino, R. E., Pazienza, G. E., Eds.; Springer, 2012.
(46) Mehonic, A.; Shluger, A. L.; Gao, D.; Valov, I.; Miranda, E.; Ielmini, D.; Bricalli, A.; Ambrosi, E.; Li, C.; Yang, J. J.; Xia, Q.; Kenyon, A. J. Silicon Oxide (SiOx): A Promising Material for Resistance Switching? *Adv. Mater.* **2018**, *30*, 1801187.
(47) Jiang, X.; Ma, Z.; Xu, J.; Chen, K.; Xu, L.; Li, W.; Huang, X.; Feng, D. a-SiNx:H-based ultra-low power resistive random access memory with tunable Si dangling bond conduction paths. *Sci. Rep.* **2015**, *5*, 15762.
(48) Yang, J. J.; Pickett, M. D.; Li, X.; Ohlberg, D. A. A.; Stewart, D. R.; Williams, R. S. Memristive switching mechanism for metal/oxide/metal nanodevices. *Nat. Nanotechnol.* **2008**, *3*, 429−433.
(49) Wang, X.; Shao, Q.; Ku, P. S.; Ruotolo, A. A memristive diode for neuromorphic computing. *Microelectron. Eng.* **2015**, *138*, 7−11.
(50) van de Burgt, Y.; Gkoupidenis, P. Organic materials and devices for brain-inspired computing: From artificial implementation to biophysical realism. *MRS Bull.* **2020**, *45*, 631−640.
(51) Mirshojaeian Hosseini, M. J.; Donati, E.; Yokota, T.; Lee, S.; Indiveri, G.; Someya, T.; Nawrocki, R. A Organic electronics Axon-Hillock neuromorphic circuit: towards biologically compatible, and physically flexible, integrate-and-fire spiking neural networks. *J. Phys. D: Appl. Phys.* **2021**, *54*, 104004.
(52) Li, B.; Hui, W.; Ran, X.; Xia, Y.; Xia, F.; Chao, L.; Chen, Y.; Huang, W. Metal halide perovskites for resistive switching memory devices and artificial synapses. *J. Mater. Chem. C* **2019**, *7*, 7476−7493.
(53) Harikesh, P. C.; Febriansyah, B.; John, R. A.; Mathews, N. Hybrid organic—inorganic halide perovskites for scaled-in neuromorphic devices. *MRS Bull.* **2020**, *45*, 641−648.
(54) Solanki, A.; Guerrero, A.; Zhang, Q.; Bisquert, J.; Sum, T. C. Interfacial Mechanism for Efficient Resistive Switching in Ruddlesden-Popper Perovskites for Non-Volatile Memories. *J. Phys. Chem. Lett.* **2020**, *11*, 463−470.
(55) Kim, S. G.; Van Le, Q.; Han, J. S.; Kim, H.; Choi, M.-J.; Lee, S. A.; Kim, T. L.; Kim, S. B.; Kim, S. Y.; Jang, H. W. Dual-Phase All-Inorganic Cesium Halide Perovskites for Conducting-Bridge Memory-Based Artificial Synapses. *Adv. Funct. Mater.* **2019**, *29*, 1906686.
(56) Zhao, X.; Xu, H.; Wang, Z.; Lin, Y.; Liu, Y. Memristors with organic-inorganic halide perovskites. *InfoMat* **2019**, *1*, 183−210.
(57) Choi, J.; Han, J. S.; Hong, K.; Kim, S. Y.; Jang, H. W. Organic-Inorganic Hybrid Halide Perovskites for Memories, Transistors, and Artificial Synapses. *Adv. Mater.* **2018**, *30*, 1704002.

https://doi.org/10.1021/acs.jpcb.1c03905
J. Phys. Chem. B XXXX, XXX, XXX−XXX

(58) Dorf, R. C.; Bishop, R. H. *Modern Control Systems*, 13th ed.; Pearson, 2017.
(59) Chua, L. Resistance switching memories are memristors. *Appl. Phys. A: Mater. Sci. Process.* **2011**, *102*, 765−783.
(60) Abraham, I. The case for rejecting the memristor as a fundamental circuit element. *Sci. Rep.* **2018**, *8*, 10972.
(61) Bisquert, J.; Guerrero, A.; Gonzales, C. Theory of hysteresis in halide perovskites by integration of the equivalent circuit *ACS Chem. Phys. Au* **2021**, DOI: 10.1021/acsphyschemau.1c00009.
(62) Zohar, A.; Kedem, N.; Levine, I.; Zohar, D.; Vilan, A.; Ehre, D.; Hodes, G.; Cahen, D. Impedance Spectroscopic Indication for Solid State Electrochemical Reaction in $(CH_3NH_3)PbI_3$ Films. *J. Phys. Chem. Lett.* **2016**, *7*, 191−197.
(63) Fabregat-Santiago, F.; Kulbak, M.; Zohar, A.; Vallés-Pelarda, M.; Hodes, G.; Cahen, D.; Mora-Seró, I. Deleterious Effect of Negative Capacitance on the Performance of Halide Perovskite Solar Cells. *ACS Energy Lett.* **2017**, *2*, 2007−2013.
(64) Guerrero, A.; Garcia-Belmonte, G.; Mora-Sero, I.; Bisquert, J.; Kang, Y. S.; Jacobsson, T. J.; Correa-Baena, J.-P.; Hagfeldt, A. Properties of Contact and Bulk Impedances in Hybrid Lead Halide Perovskite Solar Cells Including Inductive Loop Elements. *J. Phys. Chem. C* **2016**, *120*, 8023−8032.
(65) Bisquert, J.; Garcia-Belmonte, G.; Pitarch, A.; Bolink, H. Negative capacitance caused by electron injection through interfacial states in organic light-emitting diodes. *Chem. Phys. Lett.* **2006**, *422*, 184−191.
(66) Mora-Seró, I.; Bisquert, J.; Fabregat-Santiago, F.; Garcia-Belmonte, G.; Zoppi, G.; Durose, K.; Proskuryakov, Y. Y.; Oja, I.; Belaidi, A.; Dittrich, T.; Tena-Zaera, R.; Katty, A.; Lévy-Clement, C.; Barrioz, V.; Irvine, S. J. C. Implications of the negative capacitance observed at forward bias in nanocomposite and polycrystalline solar cells. *Nano Lett.* **2006**, *6*, 640−650.
(67) Göhr, H.; Schiller, C.-A. Faraday-Impedanz als Verknüpfung von Impedanzelementen. *Z. Phys. Chem.* **1986**, *148*, 105−124.
(68) Ghahremanirad, E.; Bou, A.; Olyaee, S.; Bisquert, J. Inductive Loop in the Impedance Response of Perovskite Solar Cells Explained by Surface Polarization Model. *J. Phys. Chem. Lett.* **2017**, *8*, 1402−1406.
(69) Dualeh, A.; Moehl, T.; Tétreault, N.; Teuscher, J.; Gao, P.; Nazeeruddin, M. K.; Grätzel, M. Impedance spectroscopic analysis of lead iodide perovskite-sensitized solid-state solar cells. *ACS Nano* **2014**, *8*, 362−373.
(70) Khan, M. T.; Huang, P.; Almohammedi, A.; Kazim, S.; Ahmad, S. Mechanistic origin and unlocking of negative capacitance in perovskites solar cells. *iScience* **2021**, *24*, 102024.
(71) Alvarez, A. O.; Arcas, R.; Aranda, C. A.; Bethencourt, L.; Mas-Marzá, E.; Saliba, M.; Fabregat-Santiago, F. Negative Capacitance and Inverted Hysteresis: Matching Features in Perovskite Solar Cells. *J. Phys. Chem. Lett.* **2020**, *11*, 8417−8423.
(72) Klotz, D. Negative capacitance or inductive loop? - A general assessment of a common low frequency impedance feature. *Electrochem. Commun.* **2019**, *98*, 58−62.
(73) Taibl, S.; Fafilek, G.; Fleig, J. Impedance spectra of Fe-doped SrTiO3 thin films upon bias voltage: inductive loops as a trace of ion motion. *Nanoscale* **2016**, *8*, 13954−13966.
(74) Greenlee, J. D.; Calley, W. L.; Moseley, M. W.; Doolittle, W. A. Comparison of Interfacial and Bulk Ionic Motion in Analog Memristors. *IEEE Trans. Electron Devices* **2013**, *60*, 427−432.
(75) Lanza, M.; Wong, H. S. P.; Pop, E.; Ielmini, D.; Strukov, D.; Regan, B. C.; Larcher, L.; Villena, M. A.; Yang, J. J.; Goux, L.; et al. Recommended Methods to Study Resistive Switching Devices. *Adv. Electron. Mater.* **2019**, *5*, 1800143.
(76) Brette, R.; Gerstner, W. Adaptive exponential integrate-and-fire model as an effective description of neuronal activity. *J. Neurophysiol.* **2005**, *94*, 3637−3642.
(77) Touboul, J.; Brette, R. Dynamics and bifurcations of the adaptive exponential integrate-and-fire model. *Biological Cybernetics* **2008**, *99*, 319.
(78) Ashida, G.; Nogueira, W. Spike-Conducting Integrate-and-Fire Model. *eNeuro* **2018**, *5*, ENEURO.0112-18.2018.
(79) Górski, T.; Depannemaecker, D.; Destexhe, A. Conductance-Based Adaptive Exponential Integrate-and-Fire Model. *Neural Computation* **2021**, *33*, 41−66.
(80) Fardet, T.; Ballandras, M.; Bottani, S.; Métens, S.; Monceau, P. Understanding the Generation of Network Bursts by Adaptive Oscillatory Neurons. *Front. Neurosci.* **2018**, *12*, 41.
(81) Barranca, V. J.; Johnson, D. C.; Moyher, J. L.; Sauppe, J. P.; Shkarayev, M. S.; Kovačič, G.; Cai, D. Dynamics of the exponential integrate-and-fire model with slow currents and adaptation. *J. Comp. Neurosci.* **2014**, *37*, 161−180.
(82) Naud, R.; Marcille, N.; Clopath, C.; Gerstner, W. Firing patterns in the adaptive exponential integrate-and-fire model. *Biological Cybernetics* **2008**, *99*, 335.
(83) Karantonis, A.; Nakabayashi, S. Phase flow deformations and coupled electrochemical oscillators. *Chem. Phys. Lett.* **2001**, *347*, 133−137.
(84) Rotstein, H. G. Preferred frequency responses to oscillatory inputs in an electrochemical cell model: Linear amplitude and phase resonance. *Phys. Rev. E* **2013**, *88*, 062913.
(85) Fourcaud-Trocmé, N.; Hansel, D.; van Vreeswijk, C.; Brunel, N. How Spike Generation Mechanisms Determine the Neuronal Response to Fluctuating Inputs. *J. Neurosci.* **2003**, *23*, 11628−11640.
(86) Koper, M. T. M.; Sluyters, J. H. Instabilities and oscillations in simple models of electrocatalytic surface reactions. *J. Electroanal. Chem.* **1994**, *371*, 149.
(87) Koper, M. T. M. Non-linear phenomena in electrochemical systems. *J. Chem. Soc., Faraday Trans.* **1998**, *94*, 1369.
(88) Glarum, S. H.; Marshall, J. H. The Anodic Dissolution of Copper into Phosphoric Acid: II. Impedance Behavior. *J. Electrochem. Soc.* **1985**, *132*, 2878−2885.
(89) Sadkowski, A.; Dolata, M.; Diard, J.-P. Kramers-Kronig Transforms as Validation of Electrochemical Immittance Data Near Discontinuity. *J. Electrochem. Soc.* **2004**, *151*, E20.
(90) Malmivuo, J.; Plonsey, R. *Bioelectromagnetism: Principles and Applications of Bioelectric and Biomagnetic Fields*; Oxford University Press: 1995. DOI: 10.1093/acprof:oso/9780195058239.001.0001
(91) Kandel, E. R. Principles of neural science. *Q. Rev. Biol.* **2013**, *88*, 139.